

# Experimental determination of the microscopic origin of magnetism in parent iron pnictides

D. Hsieh,<sup>1</sup> Y. Xia,<sup>1</sup> L. Wray,<sup>1</sup> D. Qian,<sup>1</sup> K.K. Gomes,<sup>1</sup> A. Yazdani,<sup>1</sup> G.F. Chen,<sup>2</sup> J.L. Luo,<sup>2</sup> N.L. Wang,<sup>2</sup> and M.Z. Hasan<sup>1,3</sup>

<sup>1</sup>*Joseph Henry Laboratories of Physics,*

*Princeton University, Princeton, NJ 08544, USA*

<sup>2</sup>*Beijing National Laboratory for Condensed Matter Physics,*

*Institute of Physics, Chinese Academy of Sciences, Beijing 100080, P.R. China*

<sup>3</sup>*Princeton Center for Complex Materials,*

*Princeton University, Princeton, NJ 08544, USA\**

(Dated: October 24, 2018)

---

\*Electronic address: mzhasan@Princeton.edu

Like high  $T_c$  cuprates, the newly discovered iron based superconductors lie in close proximity to a magnetically ordered parent phase [1, 2, 3, 4, 5], suggesting its superconductivity might be related to the mechanism driving its magnetism. However, while the magnetic order in parent cuprates is known to derive from a spin-spin interaction between electrons that are localized due to strong Coulomb repulsion [6], a plethora of experiments including neutron scattering [4, 5] have so far been unable to conclusively resolve whether a local moment Heisenberg description applies in parent iron based compounds [1, 7, 8, 9, 10], or whether magnetism arises from a collective spin-density-wave (SDW) order instability of an itinerant electron system like in chromium [11]. These two alternatives can in principle be distinguished by measuring the low energy momentum-resolved bulk-representative electronic structure of the magnetically ordered phase. However, whereas a single electronic band formed by one type of copper  $d$ -orbital contributes to the low energy electronic structure of the cuprates, the iron based compounds exhibit a complex multi-band manifold involving all five iron  $d$ -orbitals [10, 12, 13, 14], making it challenging to experimentally track the dynamics of the electrons in the bands individually and identify the ones critical to the mechanism of magnetic and superconducting ordering. Using a combination of polarization dependent angle-resolved photoemission spectroscopy (ARPES) and scanning tunneling microscopy (STM), we have isolated the complete low-lying bulk representative electronic structure of magnetic  $\text{SrFe}_2\text{As}_2$  with  $d$ -orbital symmetry specificity for the first time. Our results show that while multiple bands with different iron  $d$ -orbital character indeed contribute to charge transport, only one pair of bands with opposite mirror symmetries microscopically exhibit an itinerant SDW instability with energy scales on the order of 50 meV. The orbital resolved band topology below  $T_{SDW}$  point uniquely to a nesting driven band hybridization mechanism of the observed antiferromagnetism in the iron pnictides, and is consistent with an unusual anisotropic nodal-density-wave state. In addition, these results place strong constraints on many theories of pnictide superconductivity that require a local moment quantum magnetism starting point.

Recent bulk measurements such as the quantum oscillation [17] and optical [16] measurements on SrFe<sub>2</sub>As<sub>2</sub> support a spin-density-wave ground state where Fermi surface is directly involved, in sharp contrast to the ARPES studies [18, 19, 20] that claim an absence of SDW gaps and argue for a local superexchange Heisenberg-type mechanism of magnetism. Since ARPES is a surface sensitive technique, it has been suggested that ARPES signals may not reflect bulk physics due to surface reconstruction or contamination effects. Here we show that bulk representative signals can in fact be isolated for the iron pnictides by comparing to STM surface topography results while combined with orbital-resolved polarized photoelectron signals.

SrFe<sub>2</sub>As<sub>2</sub> undergoes both a bulk structural and magnetic phase transition at  $T_M = 190$  K, where the crystal structure changes from tetragonal to orthorhombic and antiferromagnetic order with wave vector  $\mathbf{Q}_{AF} = (\pi, 0)$  is achieved [5]. STM studies have shown that low temperature cleaved surfaces of the AFe<sub>2</sub>As<sub>2</sub> ( $A = \text{Ba, Sr, Ca}$ ) family consist of a nearly complete  $A$  layer sitting atop an As square lattice layer [22, 23], and that the surface  $A$  layer exhibits a reconstruction with wave vector  $\mathbf{Q}_{SR} = (\pi/2, \pi/2)$  (Fig. 1a,b,e). An ARPES intensity map taken at the Fermi level ( $E_F$ ) of a 10 K cleaved sample is displayed in Fig. 1c, which shows features at  $\Gamma = (0, 0)$  and  $M = (\pi, 0), (0, \pi)$  in accordance with bulk band structure calculations [10, 12, 13, 15, 24]. However there is an additional pocket centered about  $X = (\pi/2, \pi/2)$  that does not appear in any calculation. To show that this X pocket arises from a band folding due to the surface reconstruction, we first note that its geometry resembles that of the pocket enclosing  $\Gamma$  and that it locates exactly at  $\Gamma + \mathbf{Q}_{SR}$ . Second, upon raising the temperature above  $T_M$ , the surface reconstruction of Sr loses its long-range coherence (Fig. 1f), concurrent with the disappearance of the ARPES feature at X (Fig. 1d). Although the ARPES features at  $\Gamma$  and  $M$  become less sharp after thermal cycling due to surface contamination, they are largely insensitive to changes in surface atomic arrangement, providing further evidence that these states are bulk representative. Having isolated the bulk derived states, we proceed to investigate their temperature dependence (see SI for detailed study). Figures 1g-j show the evolution of the electronic structure along the  $\Gamma$ - $M$  direction through a temperature cycle across  $T_M$ . While bands  $\alpha_1$  and  $\alpha_2$  seem to simply broaden as the sample is heated, half of the parabolic bands ( $\alpha_3$  and  $\alpha_4$ ) that exhibit mirror symmetry about  $k_x \approx (0, -\pi/2)$  at low temperatures disappear above  $T_M$ . Upon cooling back to 10 K, only the  $\alpha_3$  band reappears with much stronger intensity compared to  $\alpha_4$ . Such behavior

suggests that the  $\alpha_3$  and  $\alpha_4$  bands may originate from bulk band folding due to  $\mathbf{Q}_{AF}$ , and may belong to different domains.

In order to determine the orbital character of the near- $E_F$  electronic bands, we show ARPES spectra along the  $\Gamma$ -M ( $\parallel k_x$ ) cut taken with different incident photon polarization directions to selectively excite states with different orbital symmetry. Figures **2a,b,d,e** show that changing the electric field direction from being oriented perpendicular to ( $\mathbf{E}_s$ ) to being oriented parallel to ( $\mathbf{E}_p$ ) the  $\Gamma$ -M direction results in the complete suppression of one set of bands around M and the revelation of a new non-overlapping set. Specifically, the  $\alpha_3$  and  $\alpha_4$  bands as well as the near M segment of bands  $\alpha_1$  and  $\alpha_2$  are only visible under  $\mathbf{E}_s$  geometry (see labels in fig. **2k**). Bands  $\beta_1$  and  $\beta_2$ , on the other hand, are only visible under  $\mathbf{E}_p$  geometry. Moreover, the near  $\Gamma$  segments of bands  $\alpha_1$  and  $\alpha_2$ , seen in figures **2d,e** as a single dark band of intensity, appear polarization independent. When the electric field vector has components along all three  $x$ ,  $y$  and  $z$  directions ( $\mathbf{E}_m$ ), both sets of bands seen independently under  $\mathbf{E}_p$  and  $\mathbf{E}_s$  geometries become visible, and an additional electron-like band centered about  $\Gamma$  emerges (Fig. **2f**). Such a dramatic polarization dependence can be explained by the spatial symmetries of the near tetrahedrally coordinated Fe  $3d$  complex, which consist of nearly degenerate  $t_{2g}$  triplet  $d_{xy}$ ,  $d_{xz}$  and  $d_{yz}$  closest to  $E_F$  and a degenerate  $e_g$  doublet  $d_{x^2-y^2}$  and  $d_{z^2}$  [8, 9, 13, 25] (SI). Since  $\Gamma$ -M lies in a plane of mirror symmetry ( $xz$ -plane) in the crystal, electronic states that are even (odd) under reflection with respect to this mirror plane can only be excited by light with electric field polarization pointing in (out of) the mirror plane [21]. As the  $d_{xz}$ ,  $d_{x^2-y^2}$  and  $d_{z^2}$  orbitals have even symmetry, we conclude that bands  $\beta_1$  and  $\beta_2$  have  $d_{xz}$ ,  $d_{x^2-y^2}$  or  $d_{z^2}$  character. Similarly, we conclude that bands  $\alpha_3$ ,  $\alpha_4$  and the near M segments of bands  $\alpha_1$  and  $\alpha_2$  have  $d_{xy}$  or  $d_{yz}$  character due to their odd symmetry. The near  $\Gamma$  segments of bands  $\alpha_1$  and  $\alpha_2$  on the other hand are visible under all geometries, which indicates that they are formed by some hybridization of odd and even symmetric orbitals. The case for band  $\alpha_5$  is less clear and may involve orbitals with a larger out-of-plane extent such as  $d_{z^2}$  because a finite  $\mathbf{E}_z$  is required. Since the ARPES intensity is proportional to  $\langle \mathbf{E} \cdot \mathbf{k} \rangle$  [21], the vanishing of intensity near  $\Gamma_n = (0, 0, n2\pi)$  under  $\mathbf{E}_p$  and  $\mathbf{E}_s$  geometries is expected. The highly  $d$ -like character of all these bands is supported by first principles calculations showing little weight of As  $p$ -orbitals near  $E_F$  [26]. Our results show that polarization dependent ARPES must

be employed to exhaustively map the low energy bands of the iron pnictides, and explains the difficulty of interpreting previous single polarization ARPES studies [18, 19, 27]. The full experimental band structure shown in figure 2j,k shows qualitative resemblance to LDA calculations (Fig. 2l) but exhibits a large band width renormalization that ranges from 2-3 times (it is  $\sim 4-5$  for cuprates) depending on the band, similar to LaOFeP [27]. While strong  $k_z$  dependence may explain this discrepancy, calculations and experiment both show only very weak dispersion of all bands along  $k_z$  [13, 31]. Instead, moderate electron correlations may be at play. The experimental band structure reveals a match between the  $k_x$  extent of the odd symmetry  $\alpha_3$  pockets around  $\Gamma$  and the even symmetry  $\beta_1$  and  $\beta_2$  pockets around M. To explore this possible nesting instability, a full Fermi surface geometry is required.

ARPES intensity maps near  $\Gamma$  were collected using  $\mathbf{E}_s$  geometry to capture all the bands (see Fig. 2) and are shown in figures 3a,b at different binding energies. Due to some  $k_z$  dependence of the bands [10, 13, 31], we found that the splitting between the  $\alpha_i$  bands is largest in the third BZ using 40 eV photons (Fig. 3c,d), allowing for better resolution of the individual Fermi surface pieces. Bands  $\alpha_1$  and  $\alpha_2$  form two concentric hole Fermi surfaces enclosing  $\Gamma$ , as evidenced by their growth in size with increasing binding energy. Due to a drastic weakening of the  $\alpha_3$  band intensity away from the  $\Gamma$ -M line at  $h\nu = 40$  eV, we had to use 30 eV photons to follow its dispersion away from  $\Gamma$ -M, which compromises the resolution of the  $\alpha_1$  and  $\alpha_2$  bands. Figures 3e-h show a series of constant  $k_y$  cuts near  $\Gamma$  with  $k_y$  moving progressively away from zero. For  $k_y$  exceeding approximately  $0.05 \pi$ , the  $\alpha_3$  band is seen to drop entirely below  $E_F$ , indicating that it forms disconnected Fermi pockets that do not enclose  $\Gamma$  rather than a hole pocket that does enclose it as is the case for bands  $\alpha_1$  and  $\alpha_2$ . In order to test for possible anisotropy of bands  $\alpha_1$  through  $\alpha_4$  between the  $k_x$  and  $k_y$  directions owing to the bulk lattice distortion, we performed azimuthal cuts around the  $\Gamma$  FS in the first BZ by rotating the sample so as to keep the scattering geometry identical ( $\mathbf{E}_m$ ) for each cut Figs 3i-m. As the polar angle  $\theta$  is rotated away from  $k_x$  ( $\theta = 0^\circ$ ), bands  $\alpha_1$  and  $\alpha_2$  remain gapless and retain a nearly constant Fermi wave vector  $k_F$  up to  $\theta = 90^\circ$ . Bands  $\alpha_3$  and  $\alpha_4$  however weaken in intensity as  $\theta$  approaches  $45^\circ$  ( $\Gamma$ -X line), disappear entirely at  $45^\circ$  (Fig. 3k), and then grow more intense again as  $\theta$  approaches  $90^\circ$ . The  $k_F$  location of band  $\alpha_3$  traces the outer segment of a petal shaped FS (Fig. 3n) while the  $\alpha_5$  band never exhibits any intensity near  $E_F$ , suggesting that it does not contribute to any

FS. Altogether, these results show that there exists a largely four-fold rotation symmetric FS near  $\Gamma$  in the magnetically ordered phase, which consists of two concentric hole pockets enclosing  $\Gamma$  and petal shaped hole pockets that do not enclose  $\Gamma$  (Fig. 3n). These  $\alpha_1$ ,  $\alpha_2$  and  $\alpha_3$  pockets have sizes, ignoring their  $k_z$  dependence, of around 1.6(5)%, 2.7(9)% and 1.0(4)% of the BZ respectively, which are consistent with the two sizes 0.52% and 1.38% seen in quantum oscillation measurements [17].

The ARPES intensity distribution at  $E_F$  around M taken in  $\mathbf{E}_s$  geometry (Fig. 4a,b) reveals a diffuse diamond-shaped ring of intensity enclosing M and the outer segments of two bright petals of intensity located at either side of M along  $k_x$  (only one such spot located at  $\mathbf{k} \approx (1.3\pi, 0)$  is shown for clarity). Probing these features at higher binding energies (figs 4c,d) shows firstly that the diamond-shaped FS exhibits electron-like character while the petal FS exhibits hole-like character, and secondly that these two FS pieces are disconnected, which suggests that they originate from different bands. By comparing the shape of the petal shaped feature near M and the petal shaped feature near  $\Gamma$  (located at  $\mathbf{k} \approx (1.7\pi, 0)$ ) at all binding energies, it is clear that they are completely reflection symmetric about  $k_x = 1.5\pi$ , the BZ boundary of the magnetic unit cell, which indicates that these FS features result from a band folding due to magnetic ordering. In order to study the band origin of these Fermi surfaces, we show band dispersion spectra along several momentum space cuts near M taken in  $\mathbf{E}_s$  geometry. A cut along  $k_x$  through M (Fig. 4e) shows that the bright petal FS arises from the Fermi crossings of the  $\alpha_3$  band, while bands  $\alpha_1$  and  $\alpha_2$  do not contribute any intensity close to  $E_F$  near M along  $k_x$ . A cut along  $k_y$  through M (Fig. 4f) shows that bands  $\alpha_1$  and  $\alpha_2$  both exhibit an M-shaped dispersion whose maxima do not reach  $E_F$  (see SI for detailed analysis), and continue to sink further below  $E_F$  as  $k_x$  moves away from  $\pi$  (Fig. 4g-j), eventually giving way to the appearance of the hole-like  $\alpha_3$  and  $\alpha_4$  bands near  $E_F$ . We attribute the intensity of the diamond-shaped Fermi surface to the  $\beta_2$  band, which is observed to be present but very weak in figure 4f (see SI for clear distinction of  $\beta_2$  band), and likely explains the low temperature negative Hall coefficient [28]. Further support comes from studying the ARPES intensity distribution at  $E_F$  around M using  $\mathbf{E}_p$  geometry (Fig. 4m), under which the  $\beta_1$  and  $\beta_2$  bands appear most intense (Fig. 4k). Here, it is the inner segment rather than the outer segment of the hole petals that is strongest, marking an abrupt change of orbital character between the inner and outer halves of the petal FS. As

the Fermi crossing position of the inner segment along  $k_x$  matches well with that measured for  $\beta_1$  (Fig. 2k), we conclude that the hole petal is composed of distinct halves deriving from  $\alpha_3$  and  $\beta_1$ . A cut along  $k_y$  through M under  $\mathbf{E}_p$  geometry (Fig. 4l) shows a band dispersion very similar to the cut along  $k_x$  under  $\mathbf{E}_s$  geometry (Fig. 4e), which provides evidence that the petal FSs also exist along the  $k_y$  direction, though with far weaker intensity. Altogether, these data reveal a FS near M in the magnetically ordered phase of SrFe<sub>2</sub>As<sub>2</sub> that consists of a diamond-shaped electron pocket enclosing M approximately 3.8(8)% of the BZ in size, and four smaller petal shaped hole pockets that do not enclose M (Fig. 4n), which are very similar in shape and size to those observed around  $\Gamma$ .

The geometry of the SrFe<sub>2</sub>As<sub>2</sub> FS and the momentum dependence of its orbital character point clearly to a nesting driven SDW ground state, which can be understood starting from the high temperature LDA band structure (Fig. 5a,f). Our ARPES measurements suggest that only the  $\alpha_3$  and  $\beta_1$  bands have nearly matching  $k_F$  and thus have a significant  $(\pi, 0)$  nesting instability. Therefore in a  $\mathbf{Q}_{SDW} = (\pi, 0)$  SDW ordered phase, only the  $\alpha_3$  and  $\beta_1$  bands fold onto one another (Fig. 5b). In a conventional SDW system where two Fermi surfaces are perfectly nested, the folded bands hybridize and acquire an energy gap  $\Delta$  over the entire BZ, resulting in the complete destruction of any FS in the SDW phase [29]. However, the presence of the petal hole pockets indicates that this cannot be the case in SrFe<sub>2</sub>As<sub>2</sub>, and suggests that either i) the high temperature  $\alpha_3$  and  $\beta_1$  Fermi surfaces only partially nest due to a mismatch in shape, or ii) the entirety of the  $\alpha_3$  and  $\beta_1$  Fermi surfaces are nested but gap formation takes place anisotropically ( $\Delta_x \neq \Delta_y$ ) around it. Since the former scenario cannot explain the presence of both  $\alpha_3$  and  $\alpha_4$  bands, we pursue the latter case. Anisotropic gap formation around the nested regions as shown in figures 5c,d results in a two-fold symmetric FS with petal-like hole pockets that have the exact dual orbital character as we have observed using ARPES (Fig. 5h). Such a generic two-fold symmetric FS has recently been predicted by a 5 band model [15] and a first principles study [24]. The former study also claims that an SDW gap is not allowed to open along  $k_x$  ( $\Delta_x = 0$ ) due to the particular mirror symmetries of the system, and thus the ground state is an intrinsically nodal SDW [15]. The fact that we observe a FS with four-fold rotation symmetry rather than two-fold is very likely due to the coexistence of domains with both  $\mathbf{Q}_{SDW} = (\pi, 0)$  and  $\mathbf{Q}_{SDW} = (0, \pi)$  (Fig. 5e,i), as the photon beam used in ARPES is much larger than

the typical size of a single magnetic domain, which explains the presence and temperature dependence of both  $\alpha_3$  and  $\alpha_4$  bands (Fig. 1g-j). Although a four-fold symmetric Fermi surface can in principle be realized in the 5 band model [15], it requires a very particular combination of interaction strengths and is therefore highly unlikely. The measured gap  $\Delta_y$  (Fig. 2h) is roughly consistent with weak coupling mean-field theory, which predicts  $\Delta = 3.53 k_B T_{SDW} = 58$  meV. The gap size along the  $\mathbf{Q}_{SDW}$  direction ( $\Delta_x$ ) on the other hand is unclear since it lies above  $E_F$ .

In summary, our polarization dependent ARPES measurements, guided by STM results, reveal the full ground state electronic structure of SrFe<sub>2</sub>As<sub>2</sub> for the first time, strongly pointing to a novel orbital selective anisotropically gapped SDW state driven by moderately correlated itinerant electrons. It is likely that as doping creates a size mismatch between the  $\alpha_3$  and  $\beta_1$  pockets in the non-magnetic phase [30, 31], nesting is weakened and a competing superconducting phase emerges, which is distinct from the doped Mott insulator approach that is taken for the cuprates[6] (Note that Ref-[31] does not orbital-resolve the band topology). Residual  $(\pi,0)$  nesting fluctuations in the superconducting phase are likely bosonic modes contributing to Cooper pairing in doped iron pnictides. The experimental methods demonstrated here can be systematically applied to explore the electron behavior over the full phase diagram of pnictides and other multiband correlated electron systems.

We thank A. Pasupathy and A. Pushp for assistance with STM measurements. This work is supported by U.S. DOE/BES.

## Methods

Single crystals of SrFe<sub>2</sub>As<sub>2</sub> were prepared using the methods described in [16]. ARPES measurements were carried out at the Advanced Light Source beamlines 10.0.1 and 12.0.1 in order to exploit multiple scattering geometries. Photon energies of 30 to 40 eV photons were used resulting in energy resolutions better than 15 meV and angular resolutions better than of the 1% of the Brillouin zone. Single crystalline samples of SrFe<sub>2</sub>As<sub>2</sub> ( $T_{SDW} = 190$  K) were used for this study, which were cleaved at 10 K in chamber pressures better than 3



$\times 10^{11}$  torr unless otherwise stated.

---

- [1] C. Xu and S. Sachdev. The new iron age. *Nature. Phys.* **4**, 898-900 (2008).
- [2] Y. Kamihara, T. Watanabe, M. Hirano and H. Hosono. Iron-based layered superconductor  $\text{La}[\text{O}_{1-x}\text{F}_x]\text{FeAs}$  ( $x = 0.05-0.12$ ) with  $T_c = 26$  K. *J. Am. Chem. Soc.* **130**, 3296-3297 (2008).
- [3] F. C. Hsu *et al.* Superconductivity in the PbO-type structure  $\alpha\text{-FeSe}$ . *Proc. Nat. Acad. Sci.* **105**, 14262-14264 (2008).
- [4] C. de la Cruz *et al.*, Magnetic order close to superconductivity in the iron-based layered  $\text{LaO}_{1-x}\text{F}_x\text{FeAs}$  systems *Nature* **453**, 899 (2008).
- [5] J. Zhao *et al.* Spin and lattice structures of single-crystalline  $\text{SrFe}_2\text{As}_2$ . *Phys. Rev. B* **78**, 140504 (R) (2008).
- [6] P. A. Lee, N. Nagaosa and X.-G. Wen. Doping a Mott insulator: Physics of high-temperature superconductivity. *Rev. Mod. Phys.* **78**, 17 (2006).
- [7] G. Baskaran. Quantum string liquid state in  $\text{LaOFeAs}$  and superconductivity. Preprint at <http://arxiv.org/abs/0804.1341> (2008).
- [8] J. Wu, P. Phillips and A. H. Castro-Neto. Theory of the magnetic moment in iron pnictides. *Phys. Rev. Lett.* **101**, 126401 (2008).
- [9] Q. Si and E. Abrahams. Strong correlations and magnetic frustration in the high  $T_c$  iron pnictides. *Phys. Rev. Lett.* **101**, 076401 (2008).
- [10] F. Ma, Z.-Y. Lu and Tao Xiang. Electronic structures of ternary iron arsenides  $\text{AFe}_2\text{As}_2$  ( $\text{A}=\text{Ba}, \text{Ca}, \text{or Sr}$ ). Preprint at <http://arxiv.org/abs/0806.3526> (2008).
- [11] J. Schäfer *et al.* Direct spectroscopic observation of the energy gap formation in the spin density wave phase transition at the  $\text{Cr}(110)$  surface. *Phys. Rev. Lett.* **83**, 2069 (1999).
- [12] D. J. Singh. Electronic structure and doping in  $\text{BaFe}_2\text{As}_2$  and  $\text{LiFeAs}$ : Density functional calculations. *Phys. Rev. B* **78**, 094511 (2008).
- [13] I. A. Nekrasov, Z. V. Pchelkina and M. V. Sadovskii. Electronic structure of prototype  $\text{AFe}_2\text{As}_2$  and  $\text{ReOFeAs}$  high-temperature superconductors: a comparison. *JETP Lett.*, **88**, No. 2, 144-149 (2008).
- [14] I. I. Mazin, D. J. Singh, M. D. Johannes and M. H. Du. Unconventional sign-reversing superconductivity in  $\text{LaFeAsO}_{1-x}\text{F}_x$ . *Phys. Rev. Lett.* **101**, 057003 (2008).

- [15] Y. Ran *et al.* Nodal spin density wave and band topology of the FeAs based materials. Preprint at <http://arxiv.org/abs/0805.3535> (2008).
- [16] W. Z. Hu *et al.* Origin of the spin density wave instability in  $A\text{Fe}_2\text{As}_2$  ( $A=\text{Ba}, \text{Sr}$ ) as revealed by optical spectroscopy. Preprint at <http://arxiv.org/abs/0806.2652v4> (2008).
- [17] S. E. Sebastian *et al.* Quantum oscillations in the parent magnetic phase of an iron arsenide high temperature superconductor. *J. Phys.: Condens. Matter* **20**, 422203 (2008).
- [18] L. X. Yang *et al.* Electronic structure and exotic exchange splitting in spin-density-wave states of  $\text{BaFe}_2\text{As}_2$ . Preprint at <http://arxiv.org/abs/0806.2627v2> (2008).
- [19] Y. Zhang *et al.* Correlation effects of exchange splitting and coexistence of spin-density-wave and superconductivity in single crystalline  $\text{Sr}_{1-x}\text{K}_x\text{Fe}_2\text{As}_2$ . Preprint at <http://arxiv.org/abs/0808.2738v1> (2008).
- [20] C. Liu *et al.* The Fermi surface of  $\text{Ba}_{1-x}\text{K}_x\text{Fe}_2\text{As}_2$  and its evolution with doping. Preprint at <http://arxiv.org/abs/0806.3453> (2008).
- [21] S. Huefner, Photoelectron Spectroscopy, Springer-Verlag, Berlin and Heidelberg (1994).
- [22] M. C. Boyer *et al.* Scanning tunneling microscopy of the 32 K superconductor  $(\text{Sr}_{1-x}\text{K}_x)\text{Fe}_2\text{As}_2$ . Preprint at <http://arxiv.org/abs/0806.4400> (2008).
- [23] Y. Yin *et al.* Scanning tunneling spectroscopy and vortex imaging in the iron-pnictide superconductor  $\text{BaFe}_{1.8}\text{Co}_{0.2}\text{As}_2$ . Preprint at <http://arxiv.org/abs/0810.1048> (2008).
- [24] J. Dong *et al.* Competing orders and spin-density-wave instability in  $\text{La}(\text{O}_{1-x}\text{F}_x)\text{FeAs}$ . *Europhys. Lett.* **83**, 27006 (2008).
- [25] M. J. Calderon, B. Valenzuela and E. Bascones. Effect of the tetrahedral distortion on the electronic properties of iron-pnictides. Preprint at <http://arxiv.org/abs/0810.0019v2> (2008).
- [26] C. Cao, P. J. Hirschfeld and H.-P. Cheng. Proximity of antiferromagnetism and superconductivity in  $\text{LaFeAsO}_{1-x}\text{F}_x$ : Effective Hamiltonian from ab initio studies. *Phys. Rev.* **B77**, 220506 (2008).
- [27] D. H. Lu *et al.* Electronic structure of the iron-based superconductor  $\text{LaOFeP}$ . *Nature* **455**, 81-84 (2008).
- [28] G. F. Chen *et al.* Transport and anisotropy in single-crystalline  $\text{SrFe}_2\text{As}_2$  and  $A_{0.6}\text{K}_{0.4}\text{Fe}_2\text{As}_2$  ( $A = \text{Sr}, \text{Ba}$ ) superconductors. Preprint at <http://arxiv.org/abs/0806.2648> (2008).
- [29] G. Gruner. *Density waves in solids*, Addison-Wesley Publishing Company (1994).
- [30] L. Wray *et al.* Momentum dependence of superconducting gap, strong-coupling dispersion

kink, and tightly bound Cooper pairs in the high-Tc  $(\text{Sr,Ba})_{1-x}(\text{K,Na})_x\text{Fe}_2\text{As}_2$  superconductors. *Phys. Rev. B* **78**, 184508 (2008). [⟨http://arxiv.org/abs/0808.2185⟩](http://arxiv.org/abs/0808.2185) (2008).

- [31] V. B. Zabolotnyy *et al.* Unexpected Fermi surface topology in the new pnictide superconductor. Preprint at [⟨http://arxiv.org/abs/0808.2454⟩](http://arxiv.org/abs/0808.2454) (2008).

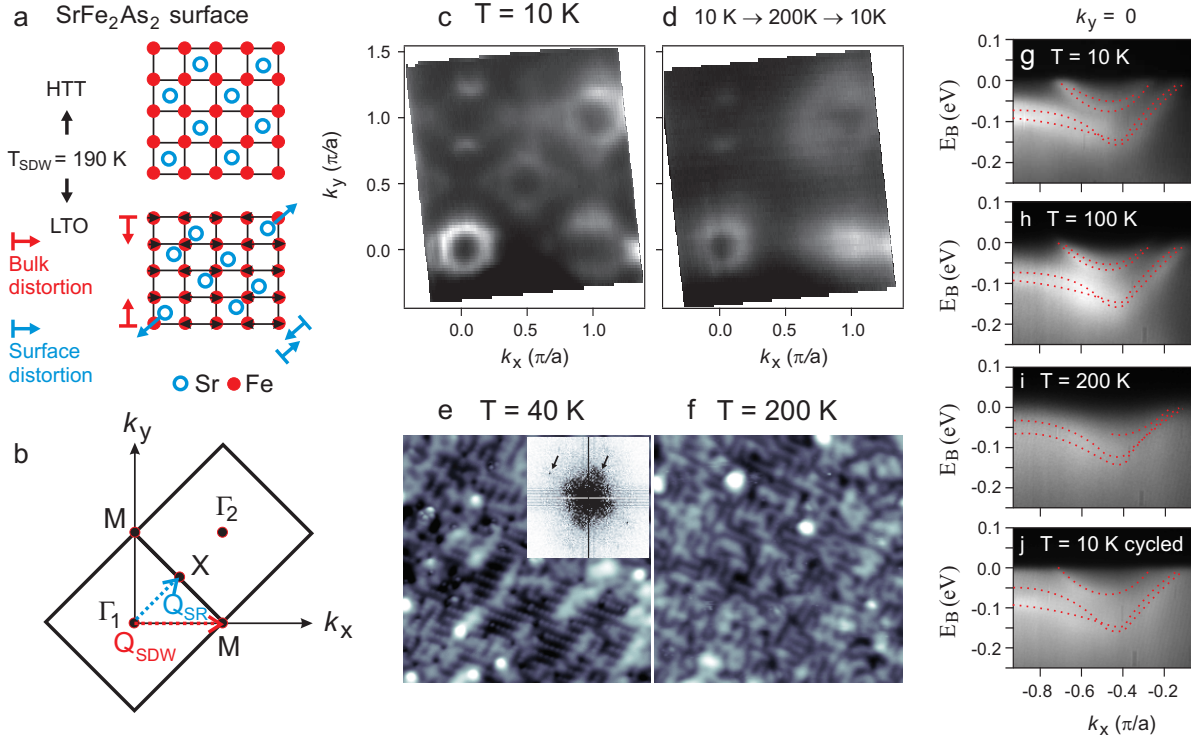
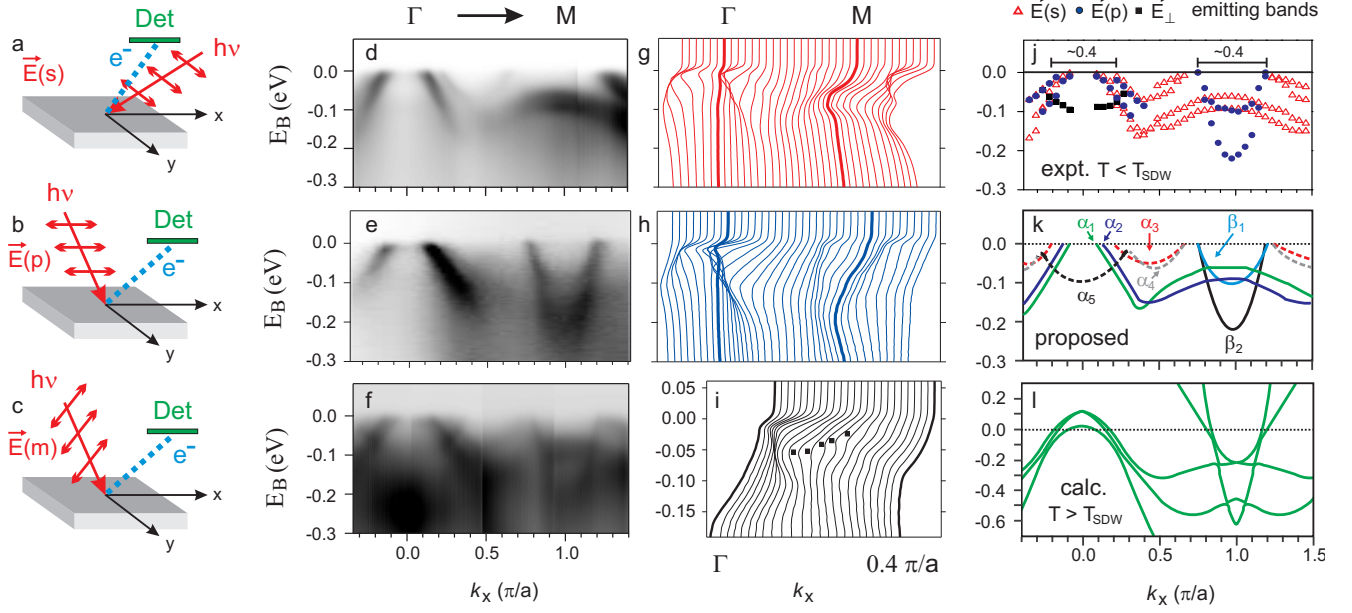
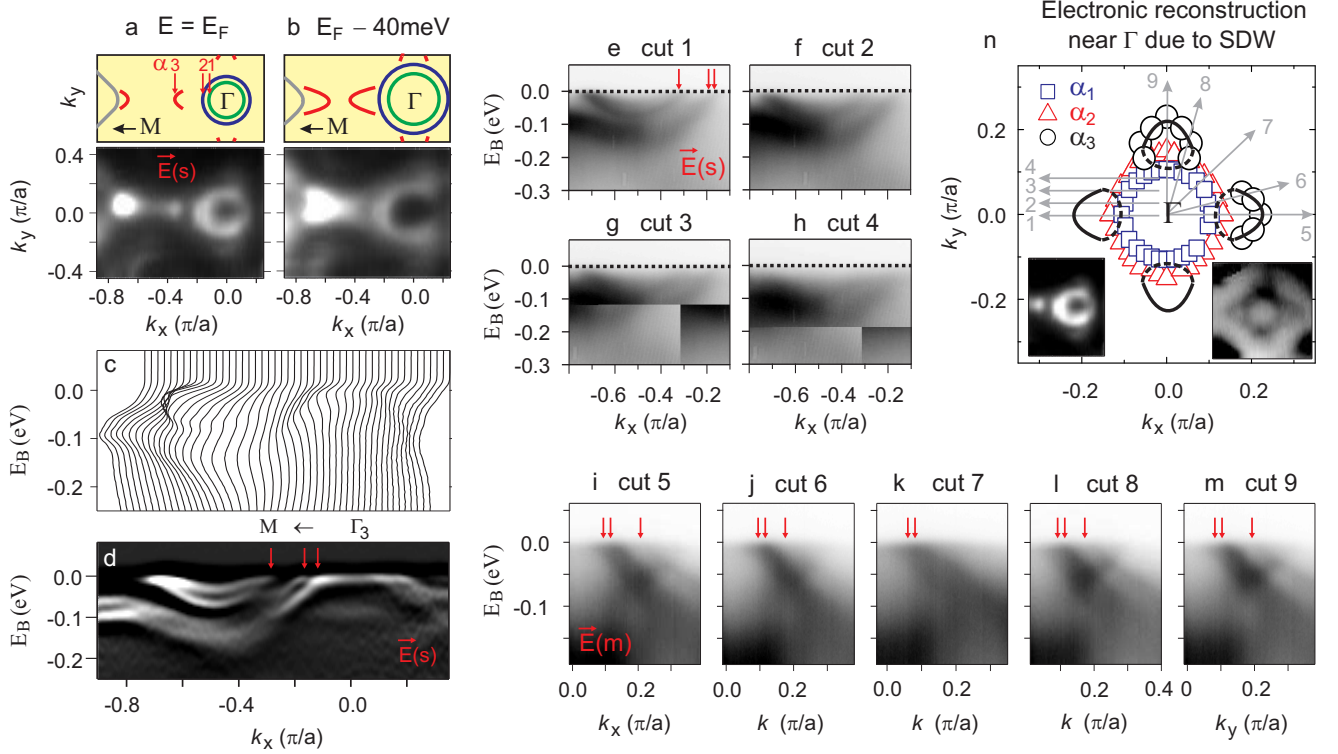


FIG. 1: **Temperature dependent study of near surface electronic structure of  $\text{SrFe}_2\text{As}_2$ .**

**a**, Schematic of the top-most layers of the crystal structure of  $\text{SrFe}_2\text{As}_2$  in the high temperature (non-magnetic) tetragonal phase and in the low temperature (magnetically ordered) orthorhombic phase. The Sr atoms are situated above the Fe plane and an intermediate As layer has been omitted for clarity. The direction of the spins in the orthorhombic phase are shown as black arrows on top of the red dots. **b**, Brillouin zones showing the wave vectors characterizing the bulk SDW ordering and surface reconstruction (SR). **c**, ARPES intensity maps taken at  $E_F$  following cleavage of the sample at 10 K and **d**, subsequent thermal cycling above  $T_M=190\text{K}$ , which removes the pocket at X. **e**, STM topograph of the surface ( $200 \text{ \AA}$ ) at 40 K. The inset is an fast Fourier transform profile of the topograph. The arrows point to the atomic peak and the  $2 \times 1$  reconstruction of the surface which is also directly seen from the topography image. **f**, Topograph of the surface ( $200 \text{ \AA}$ ) taken after warming the sample up to 200 K, showing a significant lack of the long-range reconstruction. **g-j**, Temperature evolution of the ARPES spectrum along the M- $\Gamma$  cut, which shows the disappearance of two top bands near Fermi level ( $\alpha_3$  and  $\alpha_4$ ) above  $T_M$  and reappearance of only one of them as the sample is cooled back below  $T_M$ .



**FIG. 2: Identification of band orbital character through polarization dependent ARPES and comparison to LDA calculation.** ARPES experimental configurations for **a**,  $\mathbf{E}_s$ , **b**,  $\mathbf{E}_p$  and **c**,  $\mathbf{E}_m$  measurement geometries. **d-f**, ARPES spectra of  $\text{SrFe}_2\text{As}_2$  recorded at 10 K along the  $\Gamma$ -M cut, taken under respective geometries. **g-i**, The corresponding energy distribution curves. **j**, The complete low-lying band structure in the magnetically ordered phase obtained by tracing the peak positions of polarization dependent spectra. Bands that are only visible under  $\mathbf{E}_s$  geometry have parity-odd orbital symmetry, those that are only visible under  $\mathbf{E}_p$  have parity-even orbital symmetry. **k**, The proposed band connectivity derived from our experimental data. **l**, A comparison with the LDA band structure of  $\text{SrFe}_2\text{As}_2$  in the non-magnetic phase [10] shows that the measured bands exhibit a large band dependent renormalization (note energy scales), and suggests that bands  $\alpha_3$ ,  $\alpha_4$  and  $\alpha_5$  are related to the magnetically ordered phase since they are the additional bands after accounting for the surface reconstruction. These results also suggest that to understand the magnetic groundstate one needs to carry out systematic study of these bands.



**FIG. 3: Electronic reconstruction near  $\Gamma$  in the SDW magnetic phase.** **a**, ARPES intensity map at  $E_F$  and **b**,  $E_F - 40 \text{ meV}$  of  $\text{SrFe}_2\text{As}_2$  at 10 K around  $\Gamma$  point taken with 40 eV photons in  $\mathbf{E}_s$  geometry. Data were collected in the third Brillouin zone but have been mapped back to the first BZ for clarity. The schematics on top of each image show the topology of the intensity distribution observed. The red arrows point to positions of Fermi level crossings of bands  $\alpha_1$ ,  $\alpha_2$  and  $\alpha_3$  along the M- $\Gamma$  cut. **c**, Energy distribution curves along the M- $\Gamma$  direction and **d**, its corresponding second derivative image. Bands  $\alpha_1$ ,  $\alpha_2$  and  $\alpha_3$  are seen to cross  $E_F$  at the  $k_x$  positions marked by red arrows. **e-h**, ARPES spectra taken using 30 eV photons along cuts 1 to 4. *Band  $\alpha_3$  gradually sinks completely below  $E_F$  away from the  $k_y = 0$  line, which indicates that  $\alpha_3$  forms disconnected Fermi pockets that do not enclose  $\Gamma$  rather than a hole pocket that encloses  $\Gamma$ .* **i-m**, ARPES spectra taken along cuts 5 to 9 in the first BZ (panel **n**) using 35 eV photons under  $\mathbf{E}_m$  geometry. **n**, Complete Fermi surface around  $\Gamma$  obtained from ARPES cuts similar to those shown in panels (a-m). The size of the symbols shown in **n** reflect the degree of  $k_z$  dispersion exhibited by the pockets. Bottom left inset shows overall topology of the SDW reconstructed Fermi surface at  $\Gamma$  to be contrasted with the topology of the Fermi surface observed at X due to band folding from surface reconstruction. The observed Fermi surface pockets around  $\Gamma$  can be understood within a nesting mechanism shown in Fig-5

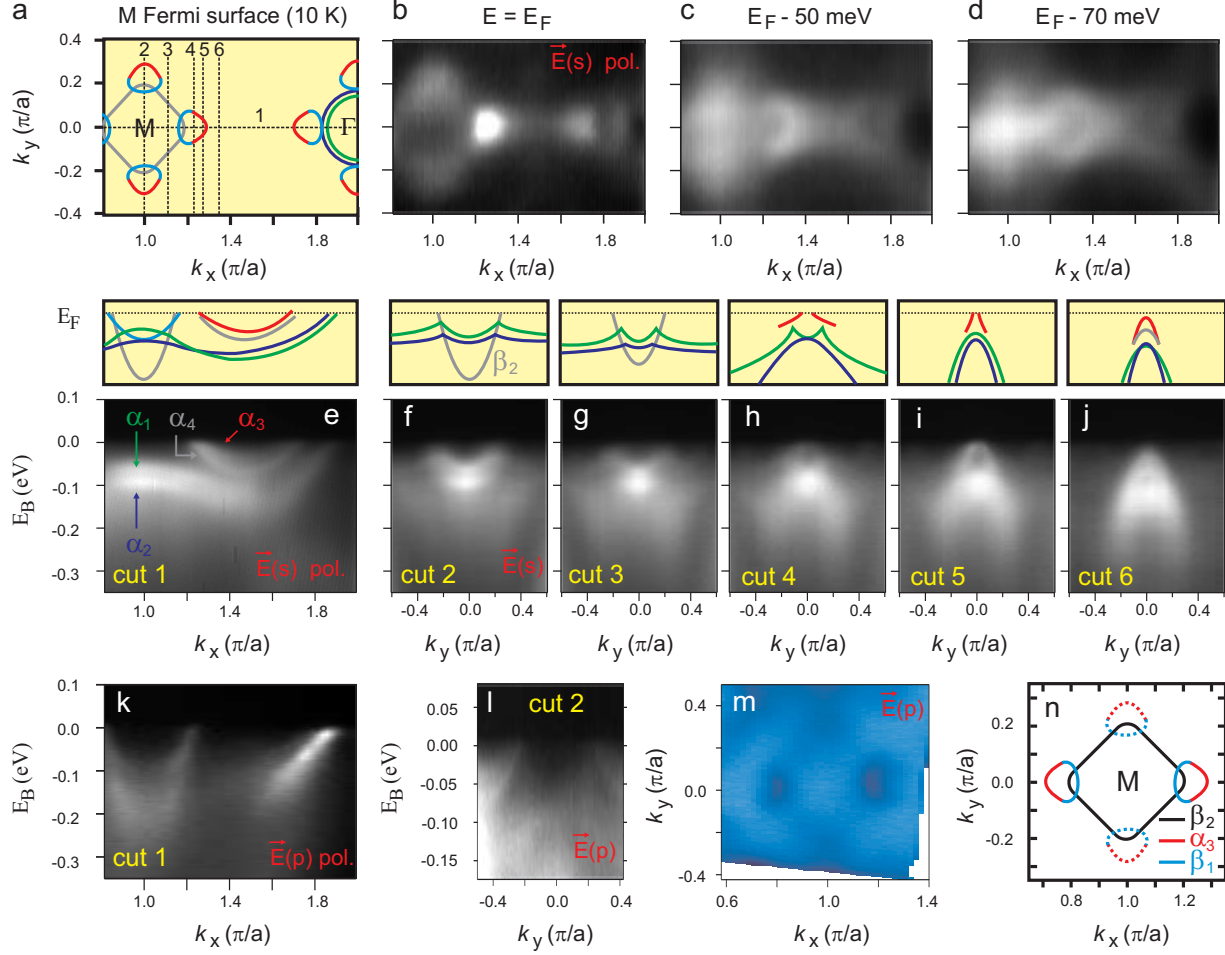


FIG. 4: **Electronic reconstruction near M in the SDW magnetic phase.** **a**, Schematic of the low temperature Fermi surface topology of SrFe<sub>2</sub>As<sub>2</sub> and the scan-line cut positions. ARPES intensity map at **b**,  $E_F$ , **c**,  $E_F - 50$  meV and **d**,  $E_F - 70$  meV taken with 30 eV photons in  $\mathbf{E}_s$  geometry at 10 K around M point, which show a diamond-shaped electron like Fermi surface enclosing M and the outer segment of a hole like Fermi pocket to its side. **e-j**, ARPES spectra taken along cut directions 1 to 6 taken in  $\mathbf{E}_s$  geometry. The schematics on top of each image show the band dispersions and the formation of the electron and hole like Fermi surfaces near M. **k**, ARPES spectrum along cut 1 and **l**, cut 2 taken with 30 eV photons under  $\mathbf{E}_p$  geometry. Band dispersion along cut 2 shows that the small hole pockets also exist along the  $k_y$  direction, though with far weaker intensity. **m**, ARPES intensity map at  $E_F$  taken under  $\mathbf{E}_p$  geometry, which reveals the inner segment of the hole pocket next to M. The fact that the diamond-shaped Fermi surface enclosing M is still visible suggests that the  $\beta_2$  band has a mixed odd and even orbital symmetry away from the  $\Gamma$ -M line. **n**, A summary of experimentally determined Fermi surface around M is presented. The dashed lines indicate that the hole pockets along  $k_y$  are observed to be far weaker than those along  $k_x$ .

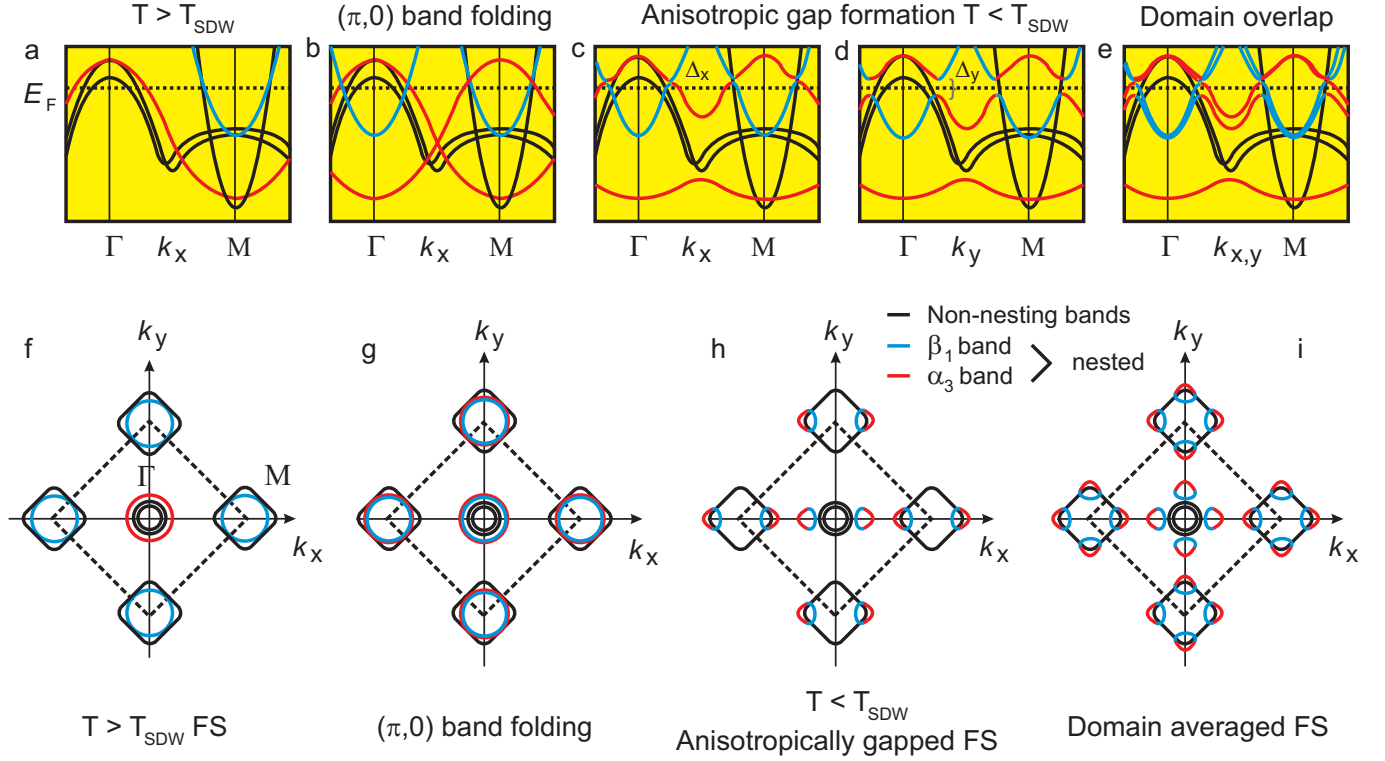


FIG. 5: **Signature of orbital dependent band nesting and an anisotropically gapped Fermi surface.** **a**, Schematic of the proposed band structure of  $\text{SrFe}_2\text{As}_2$  in the high temperature non-magnetic phase and **f**, its associated Fermi surface. The bands  $\alpha_3$  and  $\beta_1$  that are nested by  $\mathbf{Q}_{SDW}$  are shown in red and blue respectively. **b-d**, show the band folding that takes place under  $\mathbf{Q}_{SDW} = (\pi, 0)$  and a  $k_x$ - $k_y$  anisotropic gap opening that occurs following hybridization of bands  $\alpha_3$  and  $\beta_1$ . The rest of the bands (black lines) do not interact. **g-h**, Fermi surface resulting from anisotropic gap formation necessarily consists of petal shaped hole pockets made up of inner and outer segments with different orbital symmetry. **e**, Domains of both  $\mathbf{Q}_{SDW} = (\pi, 0)$  and  $(0, \pi)$  ordering in the sample give rise to the observed topology of the ARPES band structure along  $\Gamma$ -M and the shape and intensity distributions of the observed ARPES Fermi surface **i**. The schematic in **(i)** is based on the raw data presented in Fig.-3 and -4 and consistent with a recent theoretical proposal [15].